# Aqueous Corrosion Behavior of Cast CoCrFeMnNi Alloy

S. Pathak, N. Kumar, R.S. Mishra, and P.S. De

CoCrFeMnNi high-entropy alloy demonstrates good mechanical properties and can be further strengthened by thermomechanical processes. A sample alloy prepared by vacuum casting in a graphite mold was further investigated for its corrosion resistance. One-millimeter thin strips of cast alloy were used to investigate its corrosion behavior at room temperature. Linear potentiodynamic tests of the alloy in sodium chloride solution confirmed uniform corrosion property comparable to stainless steel AISI 304. However, a positive cyclic hysteresis loop indicated susceptibility to pitting corrosion. In sodium hydroxide solution, metastable pit formation was observed, while sulfuric acid solution passivated the alloy. In both cases, the alloy did not show any spontaneous pitting tendency.

## 1. Introduction

Typically, corrosion-resistant structural materials such as stainless steels or nickel-based alloys are based on a design centered on one or two principal alloying elements. In the first decade of the twenty-first century, Yeh et al. (Ref 1) advanced the concept of high-entropy alloys (HEAs) composed of multiple (4-5 or more) principal elements in equimolar or near equimolar ratios. These alloys in general show exceptional mechanical and corrosion properties compared to standard commercial alloys, with corrosion resistance in some cases exceeding that of stainless steels (Ref 2, 3). The CoCrFeMnNi HE alloy (Cantor alloy) discovered in 2004 by Brian Cantor (Ref 4) with face-centered cubic (FCC) matrix phase is reported to have encouraging fatigue characteristics and tensile ductility (Ref 5, 6). Further strengthening of this alloy is possible by mechanical and thermal processing (Ref 7, 8). Oxidation behavior of the alloy is similar to stainless steel except for its susceptibility to grain boundary oxidation and spallation tendency (Ref 9). Consequently, characterizing the aqueous corrosion resistance of Cantor alloy under different corrosive conditions is needed to evaluate its overall suitability for structural applications.

The microstructure and corrosion behavior in 1(M) $H_2SO_4$ and 1(M) NaCl solutions for CoFeNi and CoCrFeNi have already been reported (Ref 10). Both alloys have a FCC matrix with Cr-rich precipitates in the CoCrFeNi alloy (Ref 10). The corrosion current ($I_{corr}$) and corrosion potential ($E_{corr}$) obtained

from linear potentiodynamic studies suggest that both alloys have superior corrosion performance compared to AISI 304 stainless steel, with CoFeNi exhibiting the best resistance (Ref 10). More recently, a corrosion study on CoCrFeMnNi in sulfuric acid solution reported poor corrosion resistance as compared to AISI 304 stainless steel (Ref 11). In this work, the alloy used was in hot-rolled condition and water-quenched from 1200 °C, cold-rolled and further softened by heating to 900 °C for 5 min. The online inductively coupled mass spectrometer measurements on electrolyte under open circuit potential (OCP) conditions reveal a high dissolution of the individual elements, especially iron as compared to the stainless steel sample. However, the corrosion current ($I_{corr} \sim 5 \times 10^{7}$ A/cm$^2$) during cyclic polarization experiments under OCP condition is significantly low compared to stainless steel ($I_{corr} \sim 8 \times 10^{-6}$ A/cm$^2$). Further, no report on the as-cast alloy behavior as well as its corrosion resistance in chloride or alkaline conditions has been reported. The present work, therefore, investigates the corrosion resistance of the as-cast Cantor alloy comprehensively using both linear and cyclic polarization experiments for acidic (1(N) $H_2SO_4$), neutral (3.5 wt.% NaCl) and alkaline (1(N) NaOH) environments.

## 2. Experimental

High-purity Co, Cr, Fe, Mn (all 99.95% pure) and Ni (99.99% pure) metals were taken in appropriate proportions and melted in a Vacuum Induction Melting furnace to form the liquid alloy. The alloy was then cast into a graphite mold under vacuum. The cast block was further machined into thin strips of 20 mm width and 1 mm thickness and used for additional investigations as discussed below. To confirm the content of cobalt, chromium, manganese, iron and nickel in the sample, direct current plasma atomic spectrometry in accordance with ASTM E1097-12 was performed (Ref 12). Carbon and sulfur content of the alloy was measured using combustion analysis in accordance with ASTM E1941-19 (Ref 13).

### 2.1 Structural Characterization

Metallographic preparation of the HEA sample consists of rough polishing followed by fine polishing using diamond paste

S. Pathak, School of Minerals, Metallurgical and Materials Engineering, Indian Institute of Technology, Bhubaneswar, India; and Indian Institute of Technology, Hyderabad, India; N. Kumar, Department of Nuclear Engineering, North Carolina State University, Raleigh; and Department of Metallurgical and Materials Engineering, University of Alabama, Tuscaloosa; R.S. Mishra, Department of Materials Science and Engineering, University of North Texas, Denton; and P.S. De, School of Minerals, Metallurgical and Materials Engineering, Indian Institute of Technology, Bhubaneswar, India. Contact e-mail: parthasarathi.de@iitbbs.ac.in.

of 1 μm. The polished sample was etched in Glyceregia (3 ml glycerin + 2 ml HCl + 1 ml HNO₃) to reveal the parent microstructure. The surface after corrosion tests was imaged in a scanning electron microscope (SEM) using secondary electron imaging at 5 kV. X-ray diffraction (XRD) experiments using Cu Kα radiation were performed to identify crystalline phases in the alloy and to calculate lattice parameters. Further microstructural investigation using electron backscattered diffraction (EBSD) technique confirmed crystal structure and lattice parameter obtained from x-ray diffraction experiments.

### 2.2 Corrosion Testing

Linear polarization measurements were carried out in a typical three-electrode cell setup (flat cell) with the specimen acting as working electrode, a saturated calomel electrode (SCE) as reference, and platinum as a counter electrode. A 3.5 wt.% aqueous NaCl solution de-aerated with nitrogen was used as an electrolyte, and the experiments were carried out at room temperature. Nitrogen gas purging of the electrolytic solution was initiated 50 min before the start of the experiment, to remove any dissolved oxygen in the electrolyte (Ref 14). The specimen was subsequently scanned potentiodynamically starting from the OCP value at a potential sweep rate of 0.6 V h$^{-1}$ (ASTM G5). After each measurement (anodic or cathodic), the electrolyte solution was renewed, and the flat cell was washed and dried. The sample as well as the copper conductor at working electrode end was diamond-polished (3-4 μm), washed thoroughly in water and dried in ethanol. The platinum electrode tip was cleaned at regular intervals on SiO₂ powder to remove any residuals from previous experiments. A similar practice was used to test the alloy in 1(N) H₂SO₄ (pH = 0.3) and 1(N) NaOH (pH = 14) electrolytes (ASTM G5 standard). The only difference from the procedure described above was

that sample polishing was done at P600 (26 μm) compared to 3-4 μm diamond for 3.5 wt.% aqueous NaCl solution.

Susceptibility of the CoCrFeMnNi alloy to pitting corrosion was corroborated via cyclic polarization testing. As in linear polarization, the sample to be tested was polished in 3-4 μm diamond paste to a clean continuous surface devoid of discontinuities. Test preparations were similar to linear potentiodynamic experiments mentioned earlier. The OCP was determined, and a scan comprised of one full cycle starting from $E_{corr}$ to + 1.2 V, reverting to − 1.2 V, followed by reversion to $E_{corr}$ was completed. The full test cycle was done at a rate of 0.00017 V per second (0.6 V per hour), and the graph of absolute current density versus potential was plotted. Similar cyclic testing was done in 1(N) H₂SO₄ and 1(N) NaOH solutions. The only change effected was in the polishing of the sample, which was performed with P600 grit emery paper. In these experiments, the cycle was reversed before current value reached 5 mA (the oxygen evolution potential), as suggested in ASTM G61.

## 3. Results

### 3.1 Microstructure

Optical micrograph of the as-cast high-entropy alloy in Fig. 1(a) shows a dendritic structure typical of a cast sample. Figure 1(b), an electron backscattered diffraction map of the sample, displays large grain sizes typical of solidified structures with low-angle boundaries distributed homogeneously within. The low-angle boundaries are designated by thin black lines, while the high-angle grain boundaries are designated by thick black lines. Another distinctive feature is sporadic small grain-
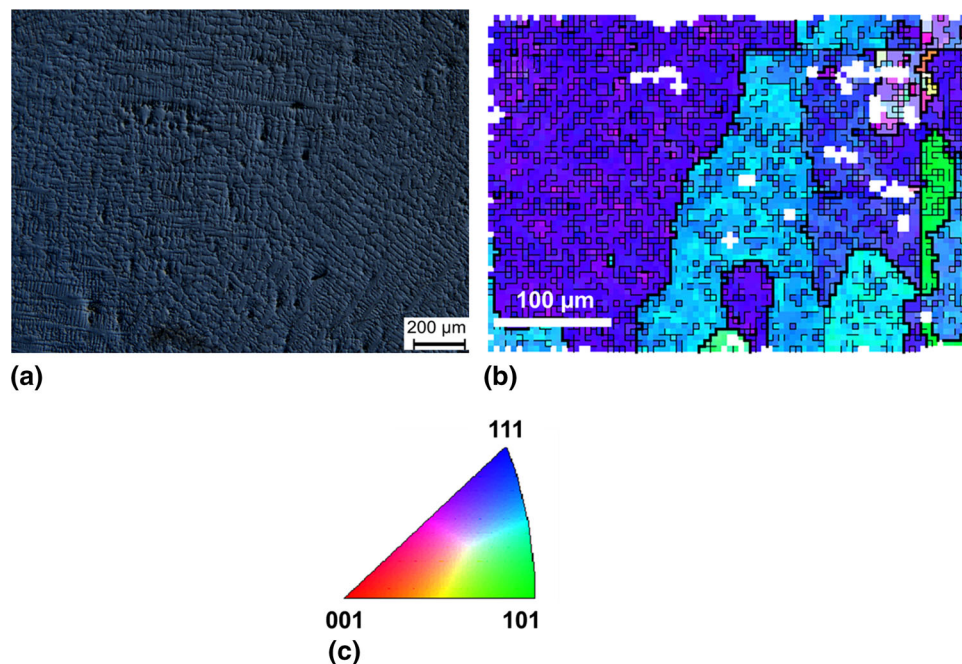


**Fig. 1** (a) Optical micrographs of as-cast alloy. (b) EBSD map of as-cast alloy showing the grains and grain boundaries in inverse pole figure coloring. The white areas are unresolved regions. (c) Legend for inverse pole figure coloring

like structures within the big grains, the possible consequence of which is explained in Sect. 4.2.

### 3.2 EDS and Chemical Analysis

The average chemical composition of the prepared alloy is given in Table 1. Carbon and sulfur content measured in weight percent using combustion analysis was $0.05 \pm 0.01\%$ and $0.01 \pm 0.005\%$, respectively. EDS mapping of the etched sample (Fig. 2) illustrates an increased concentration of nickel and manganese in the interdendritic region, while cobalt, chromium and iron are preferentially located within the dendrites.

### 3.3 X-ray Diffraction Analysis

The x-ray diffraction pattern of the as-cast material is shown in Fig. 3. The indexed pattern confirms a predominantly single-phase FCC crystal structure with a lattice parameter of 3.59 $\mathring{A}$. (Lattice parameter of Cu is 3.61 $\mathring{A}$.) X-ray diffraction experiments performed on corroded samples exhibit no additional peaks, an indication that corrosion products formed are below the detection limit of x-ray diffraction.

### 3.4 SEM Analysis

Scanning electron micrographs of the CoCrFeMnNi alloy for both uncorroded (Fig. 4a) and corroded samples (Fig. 4b) are presented. Intermittent corroded regions are observed at

**Table 1** Mean composition of the HEA sample in weight percent as obtained from direct current plasma emission spectrometry in accordance with ASTM 1097-12. Carbon and sulfur constitute rest

| Cr | Mn | Fe | Co | Ni |
|---|---|---|---|---|
| 18.05 | 19.0 | 19.54 | 22.0 | 20.45 |

$\sim 2000X$ magnification in an otherwise continuous surface after polarization testing in 3.5 wt.% aqueous NaCl solution. The unaffected regions appearing similar to the untested samples indicate a non-uniform corrosion pattern.

### 3.5 Corrosion Testing

**3.5.1 Uniform Corrosion Testing.** The potentiodynamic polarization curves of the as-cast CoCrFeMnNi alloy in 3.5 wt.% aqueous NaCl electrolyte solution are shown in Fig. 5, with polarization curves for 304 stainless steel plotted for comparison (Ref 14). Similarly, resistance polarization experiments (range $- 25$ mV to $+ 25$ mV relative to $E_{corr}$) and slope (i.e., $\Delta E/\Delta i$ or resistance polarization) are determined by a linear fit. To obtain the anodic and cathodic Tafel slopes (i.e., $\beta_A$ and $\beta_C$, respectively), the following rules were put in place: (a) For good accuracy, at least one decade of linearity was taken in Tafel exploration. (b) The largest available range of potentials was determined. (c) Values obtained were double-checked by repeating the experiments under the same conditions. Using the values of $\beta_A$, $\beta_C$ and resistance polarization, the corrosion current ($i_{corr}$) was calculated from the Stern–Geary equation given as:

$$i_{corr} = \frac{\beta_A * \beta_C}{2.3 * (\beta_A + \beta_C)} \times \frac{\Delta i}{\Delta E} \qquad \text{(Eq 1)}$$

The mean $i_{corr}$ value is $3.83 \times 10^{-7}$ A/cm$^2$, with a standard deviation of $1.67 \times 10^{-7}$ A/cm$^2$. The corrosion rate (CR) of the alloy (i.e., penetration rate) is obtained from the $i_{corr}$ value using the following equation.

$$CR \, (\text{in mmpy}) = \frac{k * i_{corr} * e}{d} \qquad \text{(Eq 2)}$$

where $i_{corr}$ is given in microamperes (μA), $k$ is a constant defining the unit for corrosion rate (for mmpy, $k = 3.27 \times 10^{-3}$), $d$ is alloy density ($\sim 7.97$ gm/cc), and $e$ is the equivalent weight given as:
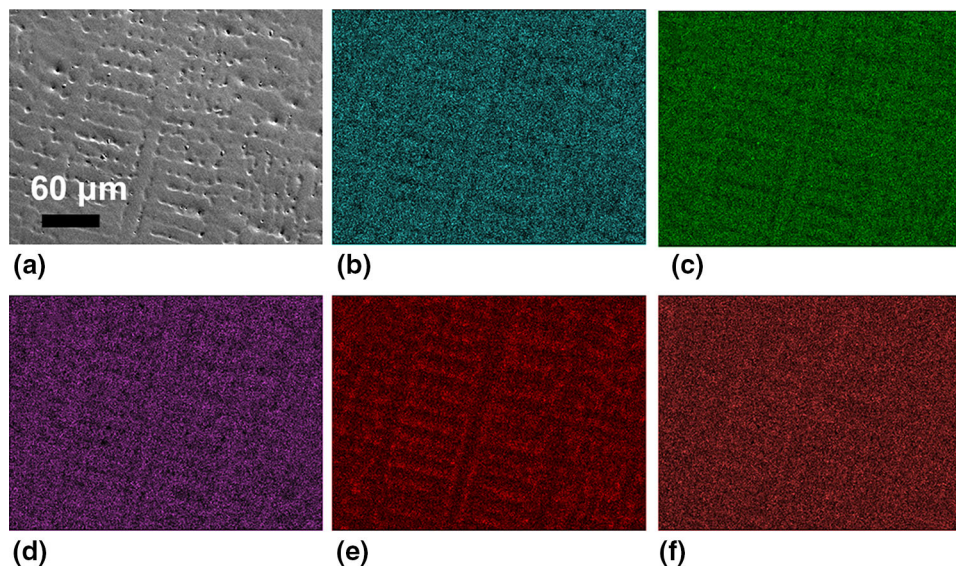


**Fig. 2** Energy-dispersive spectroscopy map of the etched as-cast alloy where (a) electron image and corresponding (b) Co map, (c) Cr map, (d) Fe map, (e) Mn map, (f) Ni map. Note that marker bars are not put in figures (b–f), as they correspond to the same image of (a)

$$e = \frac{(M \cdot W)_{Fe}}{(V)_{Fe}} X_{Fe} + \frac{(M \cdot W)_{Co}}{(V)_{Co}} X_{Co} + \frac{(M \cdot W)_{Cr}}{(V)_{Cr}} X_{Cr}$$
$$+ \frac{(M \cdot W)_{Mn}}{(V)_{Mn}} X_{Mn} + \frac{(M \cdot W)_{Ni}}{(V)_{Ni}} X_{Ni} \quad \text{(Eq 3)}$$

where $(M \cdot W)_i$ is the molecular weight of $i$th element, $V_i$ is the valency of element "i" (taken 2 for all), and $X_i$ is the atomic fraction of element "i" in the alloy. The equivalent weight of the given alloy is calculated as 28.02, and the corrosion rate is 0.0044 mmpy. Similar experiments on as-received specimens were carried out in 1(N) NaOH and 1(N) $H_2SO_4$ solutions (Fig. 6, 7). These results are summarized in Table 2. The potentiodynamic curve in 1(N) NaOH case reveals an interesting behavior not seen in any other environment. Here, the change in potential results in rapid fluctuation of current density, especially near the $E_{corr}$ values. This fluctuation in current near $E_{corr}$ is magnified in Fig. 8. However, such fluctuation in current density disappeared for the experiment carried out in 1(N) NaOH on the specimen passivated in 1(N) $H_2SO_4$ solution (Fig. 6b).

**3.5.2 Measurement of Non-uniform Corrosion.** To ascertain the extent of pitting corrosion in the alloy, cyclic polarization testing was done in three different environments (3.5 wt.% NaCl, 1(N) NaOH and 1(N) $H_2SO_4$). Figure 9, 10 and 11 presents the cyclic polarization curves. Table 3 gives the 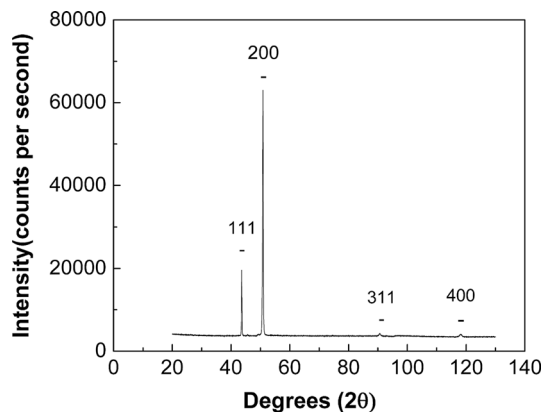pitting and protection potential in the three different test environments. For the susceptibility of CoCrFeMnNi to pitting corrosion in the basic environment (1 N NaOH), the return potential ($E_{rev}$) was kept equal to 0.7 V from $E_{corr}$ for both anodic and cathodic ends (Fig. 6). In an acidic environment (1 N $H_2SO_4$), strong passivation was observed. ($E_{pass}$ is − 0.232 V.) The passivation region was wider than that of 304 SS (Fig. 12).

## 4. Discussion

### 4.1 Microstructure and Phases Present

The microstructure of the cast CoCrFeMnNi is a dendritic structure (Fig. 1), any of which is expected to have microsegregation. Thus, EDS results (Fig. 2) provide clear evidence of nickel and manganese segregation into the interdendritic regions, while cobalt, iron and chromium were enriched within the dendrites. The result is in contrast to Vaidya et al. (Ref 15), who reported only manganese microsegregation. The sample preferentially corrodes (pitting type) from the interdendritic region as is clear in the SEM image of the corroded sample after aqueous NaCl exposure (Fig. 13). The x-ray diffraction



**Fig. 5** The linear polarization experiment plot for CoCrFeMnNi alloy exposed to 3.5 wt.% aqueous NaCl solution. The 304 SS curve is given for comparison



**Fig. 3** X-ray diffraction pattern of as-cast CoCrFeMnNi alloy
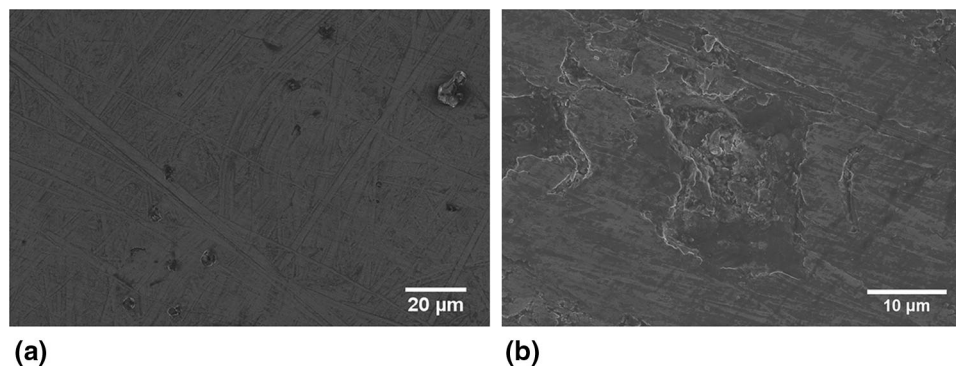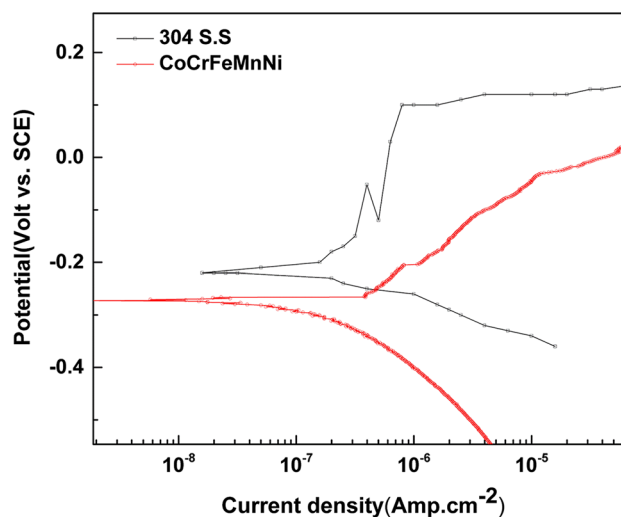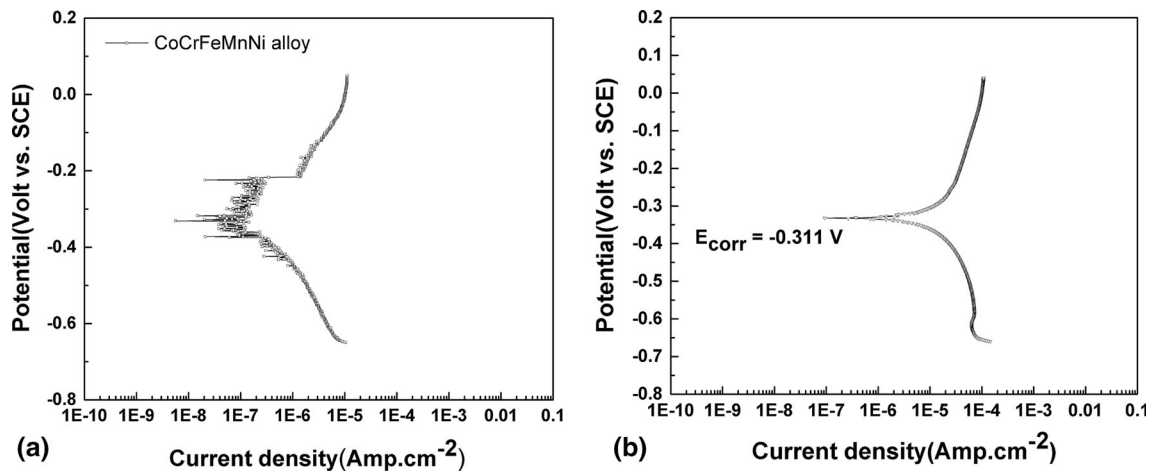


**Fig. 4** SEM images of CoCrFeMnNi (a) before corrosion and (b) after corrosion in 3.5 wt.% aqueous NaCl solution. Note the pits formed after exposure to NaCl solution

**Fig. 6** Polarization curves for CoCrFeMnNi in (a) 1(N) NaOH and (b) NaOH after passivation in 1(N) $H_2SO_4$
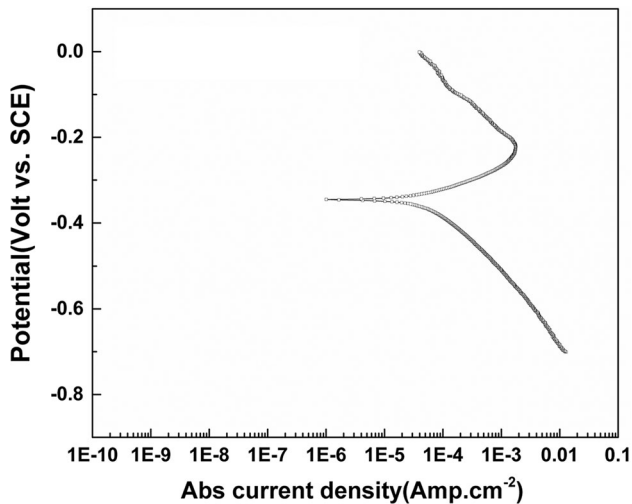


**Fig. 7** Polarization curves for CoCrFeMnNi in 1(N) $H_2SO_4$

**Table 2 Results from linear polarization experiments**

| Solution used | $E_{corr}$, V | $I_{corr}$, A/cm$^2$ | Corrosion rate, mmpy |
|---|---|---|---|
| 3.5 wt.% NaCl | $-0.26 \pm 0.02$ | $3.8 \times 10^{-7} \pm 1.7 \times 10^{-7}$ | 0.0044 |
| 1(N) NaOH | $-0.33 \pm 0.02$ | $1.7 \times 10^{-6} \pm 2.7 \times 10^{-5}$ | 0.0191 |
| 1(N) $H_2SO_4$ | $-0.36 \pm 0.02$ | $1.2 \times 10^{-4} \pm 3.1 \times 10^{-5}$ | 1.425 |

pattern indicating the presence of one single FCC phase suggests that both dendritic and interdendritic regions are of the same crystalline structure. The low carbon and sulfur content of the alloy confirms that insignificant pickup of carbon from graphite mold has occurred during casting.

### 4.2 Corrosion in 3.5 wt.% Sodium Chloride Solution

The uniform corrosion susceptibility of CoCrFeMnNi alloy in sodium chloride solution is more or less similar to AISI 304 stainless steel alloy (0.383 μA/cm$^2$ compared to 0.61 μA/cm$^2$).

But, its susceptibility to localized corrosion is clearly observed in the cyclic polarization curve. A positive hysteresis curve where reverse current density exceeds forward scan current density indicates pitting corrosion (Ref 16). The pitting potential value ($E_{pit}$) is 0.17 V, and the difference between pitting and protection potential is 0.63 V. The protection potential being less than the OCP value indicates spontaneous pitting corrosion. During pitting corrosion in chloride solution, pit nucleation is considered to be an outcome of volume expansion and rupture of protective film interface caused by chloride migration from the electrolyte to the metal–film interface (Ref 17). The nucleated pit repassivates or propagates, depending on availability of the electrolyte (Ref 18). If the current is high enough and/or the pit opening is sufficiently obstructed (e.g., by remnants of the ruptured oxide film), the embryonic pit may develop into a metastable pit (Ref 19). In the metastable state, pit growth depends on site geometry and the surrounding passive film. Once the pit propagates metastably to a sufficient size, it reaches a state where pit growth is stabilized and the pit propagates indefinitely. This potential for the start of stable pit growth, which is the last step in pit growth kinetics, indicates the transition from metastable growth state and defines the pitting potential. However, the cyclic curve of CoCrFeMnNi alloy exhibits no metastable pitting and thus confirms that the primary embryonic pit is developing directly into stable pits.

At $E_{pit}$ (Fig. 9), the sudden rise in current density to $\sim$ 5 mA in an extremely small voltage range indicates the passage of current through fresh surface generated within the pits. According to the accepted pitting mechanism (Ref 20, 21), Cl$^-$ anions diffuse through the passive oxide layer to the metal substrate as assisted by oxygen vacancies. Simultaneously, Fe and other elements with + 2 oxidation states present in the alloy form Schottky pairs at the surface. The cation vacancies formed due to electrolytic dissolution travel from the oxide–electrolyte interface toward the metal–oxide interface. The accumulation of cation vacancies within the oxide layer leads to internal stresses that weaken the oxide structure and ultimately result in pitting (Ref 22). A restriction in pit geometry and/or barriers due to corrosion products in some cases can further confine the cations within the pits (Ref 24). The resultant cation accumulation and hydrolysis will develop localized acidic regions within the pits (Ref 25). With accumulation of H$^+$ ions as well
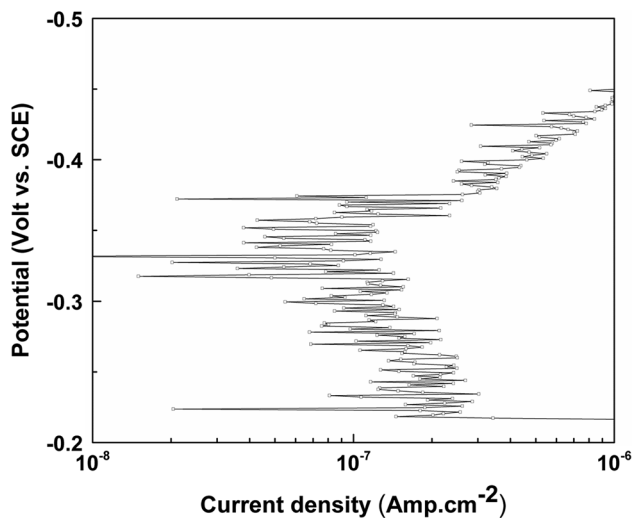
**Fig. 8** Magnification of Fig. 6(a) near $E_{corr}$, showing the fluctuation in current density
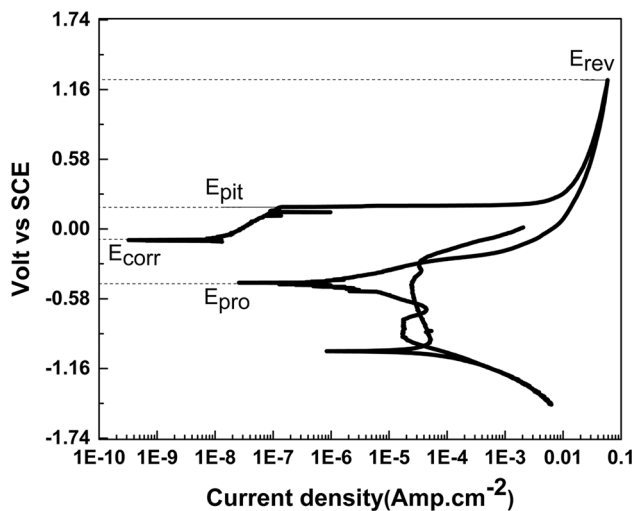


**Fig. 10** Cyclic polarization curve of CoCrFeMnNi alloy in 1(N) NaOH



**Fig. 9** Cyclic polarization curve of CoCrFeMnNi alloy in 3.5 wt.% aqueous NaCl solution



**Fig. 11** Cyclic polarization curve of CoCrFeMnNi alloy in 1(N) $H_2SO_4$

as cations within active pits, $Cl^-$ ions start migrating from the bulk electrolyte into the electrolyte present within the pits, to preserve charge neutrality (Ref 26). This migration will lead to a further increase in pit volume, and hence corrosion current and pitting become autocatalytic (Ref 26). In fact, online measurement of Cantor alloy dissolution in aqueous NaCl solution indicates a preferential dissolution of Fe under open circuit and transpassive conditions compared to Ni, Mn, Cr or Co (Ref 11). The results suggest that the $Fe^{2+}$ ions migrate preferentially into the electrolyte. The $Cl^-$ ions absorbed at anion vacancies will assist in further dissolution. The vacancies forming at metal/metal oxide interfaces will result in stresses within the passive film and in pit initiation. The small grains with high-angle boundary (Fig. 1b) within the dendritic structures will exacerbate the pit initiation phenomena (Ref 23). A schematic of this pitting model is shown in Fig. 14.

In the present alloy, with a further increase in voltage, current density rise diminishes, although no passivation is observed. This lack of passivation indicates that the oxide layer
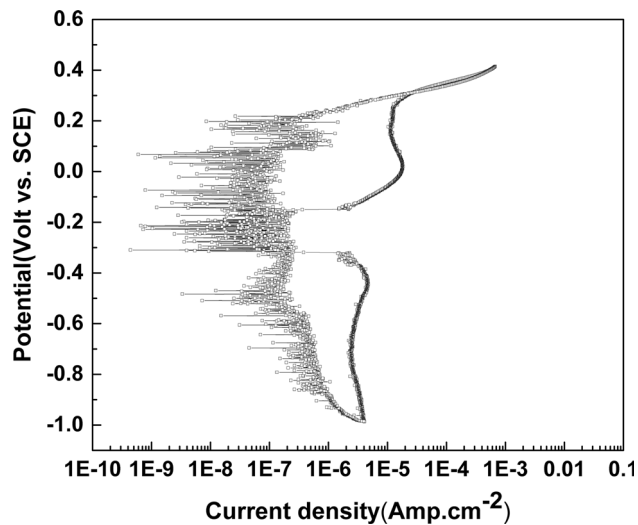
especially in the low-chromium interdendritic region (see Fig. 13), once ruptured, is never restored back on the alloy. Note that in molybdenum-containing stainless steels, the resistance to pitting corrosion is generally assessed by pitting resistance equivalent (PRE), which is expressed as (Ref 27),

$$PRE = \%Cr + 3.3 \cdot \%Mo \qquad (Eq\ 4)$$

Recent aqueous corrosion investigations in $Co_{1.5}CrFeNi_{1.5}Ti_{1.5}Mo_x$ alloys suggest that a PRE value of 26% results in negative hysteresis loop with pitting corrosion resistance (Ref

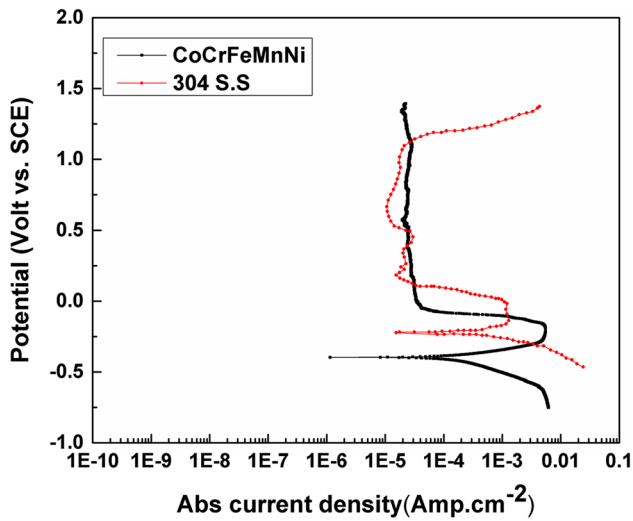**Table 3 Results from cyclic polarization experiments**

| Solution used | $E_{pit}$, V | $E_{pro}$, V |
|---|---|---|
| 3.5 wt.% NaCl | 0.17 | − 0.46 |
| 1(N) NaOH | 0.21 | − 0.15 |
| 1(N) $H_2SO_4$ | − 0.39 | − 0.39 |

**Fig. 12** A comparison of the behavior of CoCrFeMnNi and 304 SS in 1(N) $H_2SO_4$. The data for stainless steel are taken from Ref (2)
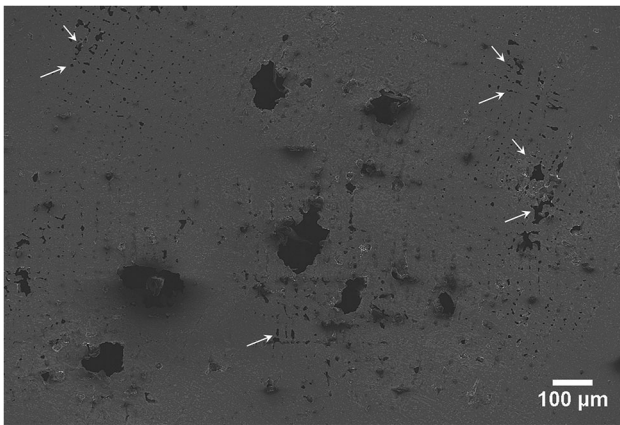


**Fig. 13** Primary electron image of the alloy exposed to 3.5 wt.% aqueous NaCl solution indicating preferential pit formation (see arrows) in the low-chromium interdendritic region
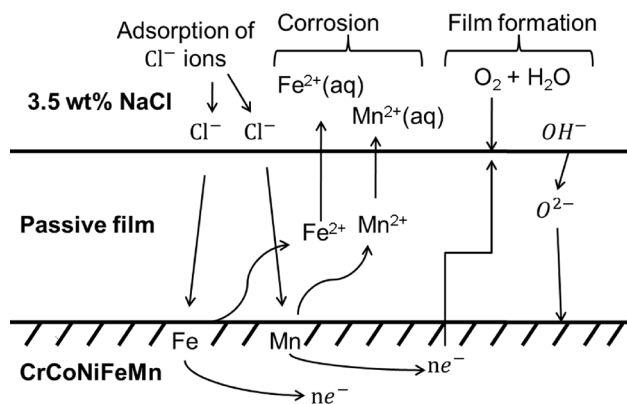


**Fig. 14** A schematic model of initiation of pitting corrosion in CoCrFeMnNi alloy in NaCl solution

28). In the present alloy, the PRE value of $\sim$ 19% suggests that optimizing the Cr content of Cantor alloy to higher values and removal of interdendritic segregation of manganese and nickel by further hot working can result in a better pitting corrosion resistance property.

### 4.3 Corrosion in 1(N) NaOH

A significant feature in both linear and cyclic polarization of CoCrFeMnNi alloy in 1(N) NaOH solution is the fluctuation of current density around the $E_{corr}$ region with change in potential. The fluctuation is explicitly visible in the polarization curves (Fig. 6b, 10), when the voltage scan is in forward direction (i.e., from negative to positive), and is typical of metastable pitting phenomena and can happen due either to (a) $Cl^-$ ions being in every chemical grade NaOH or (b) diffusion of $OH^-$ ions through the oxygen vacancies as in $Cl^-$ ions. Both $Cl^-$ and $OH^-$ ions are small (181 pm and 114 pm) and can cause corrosion at the metal/oxide interface (Ref 20, 29). The negative hysteresis loop with a pitting potential higher than $E_{corr}$ and protection potential similar to $E_{corr}$ indicates that pitting is not spontaneous and pits, if formed, will be unable to grow further (Ref 30). The fluctuation characteristic of metastable pitting is, however, completely absent when the sample is passivated by exposure to 1(N) $H_2SO_4$ (Fig. 6b). Similar results are reported for $Al_{0.3}CrFe_{1.5}MnNi_{0.5}$ alloy where anodic treatment resulted in elimination of pitting corrosion (Ref 31). The results, therefore, clearly confirm that fluctuation due to metastable pitting is a consequence of the nature of the protective layer in the given alloy.

### 4.4 Corrosion in 1(N) $H_2SO_4$

For both uniform and non-uniform corrosion tests in sulfuric acid, the corrosion current is linear and is constant up to $-$ 0.2 V (Fig. 7, 11), beyond which passivation occurs. In the case of 304 SS in 1(N) $H_2SO_4$ (Fig. 12), a similar trend is observed where gradual passivation occurs at a higher voltage and is followed by passivation with constant current density. However, in the case of CoCrFeMnNi alloy, this passivation does not undergo breakdown even at voltages as high as 1.4 V, while in 304 SS, this breakdown occurs at approximately 1.2 V. In the case of cyclic polarization tests, the reverse scan traces along the initial forward curve with small changes in current density. Thus, some part of the oxide layer formed due to repassivation at higher potential is retained along the entire cyclic scan in the direction of lower potential. The retracing of protection potential back to the $E_{corr}$ value and distinct passivation tendency suggest that pitting is not possible in this condition (Ref 30).

## 5. Conclusions

1. The as-cast HEA has unidirectional dendritic structure and an equiatomic composition with FCC crystal structure as obtained from XRD analysis.
2. The CoCrFeMnNi alloy with an $i_{corr}$ value lower than 304 SS ($3.83 \times 10^{-7}$ A/cm$^2$ < $6.01 \times 10^{-7}$ A/cm$^2$) indicates better corrosion resistance in 3.5 wt.% aqueous NaCl solution compared to 304 SS.

3. The $E_{pro}$ obtained below $E_{pit}$ suggests that CoCrFeMnNi is prone to pitting corrosion in 3.5 wt.% sodium chloride solution, especially from the interdendritic regions.

4. Tafel plot for 1(N) NaOH confirms that CoCrFeMnNi is prone to corrosion with no signs of passivation. The potentiodynamic curve showing significant fluctuations in current density indicates metastable pitting which, however, is absent in the passivated (1(N) $H_2SO_4$) sample. The material is, however, resistant to spontaneous pitting corrosion.

5. In the case of 1(N) $H_2SO_4$, the constant linear increase in the corrosion current is evident to almost $+ 0.2$ V of potential. Beyond this point, the curve shows passivation as in 304 SS. At potential higher than 1.2 V, this passivation breaks in 304 SS. However, in CoCrFeMnNi alloy, the passivation continues beyond 1.2 V. Hence, CoCrFeMnNi is more corrosion resistant in acidic environment of 1(N) $H_2SO_4$ compared to 304 SS. Cyclic polarization tests confirm that pitting potential and protection potential are equal, thereby revealing resistance to pit formation.

## References

1. J.-W. Yeh, S.K. Chen, S.J. Lin, and J.Y. Gan, Nanostructured High-Entropy Alloys with Multiple Principal Elements: Novel Alloy Design Concepts and Outcomes, *Adv. Eng. Mater.*, 2004, **6**(5), p 299–303

2. Y. Zhang, T.T. Zuo, Z. Tang, M.C. Gao, K.A. Dahmen, P.K. Liaw, and Z.P. Lu, Microstructures and Properties of High-Entropy Alloys, *Prog. Mater Sci.*, 2014, **61**, p 1–93

3. Y. Qiu, M.A. Gibson, H.L. Fraser, and N. Birbilis, Corrosion Characteristics of High Entropy Alloys, *Mater. Sci. Technol.*, 2015, **31**(10), p 1235–1243

4. B. Cantor, I.T.H. Chang, P. Knight, and A.J.B. Vincent, Microstructural Development in Equiatomic Multicomponent Alloys, *Mater. Sci. Eng. A*, 2004, **375–377**, p 213–218

5. K.V.S. Thurston, B. Gludovatz, A. Hohenwarter, G. Laplanche, E.P. George, and R.O. Ritchie, Effect of Temperature on the Fatigue-Crack Growth Behavior of the High-Entropy Alloy CrMnFeCoNi, *Intermetallics*, 2017, **88**, p 65–72

6. M.J. Yao, K.G. Pradeep, C.C. Tasan, and D. Raabe, A Novel, Single Phase, Non-equiatomic FeMnNiCoCr High-Entropy Alloy with Exceptional Phase Stability and Tensile Ductility, *Scr. Mater.*, 2014, **72**, p 5–8

7. E.J. Pickering, R. Muñoz-Moreno, H.J. Stone, and N.G. Jones, Precipitation in the Equiatomic High-Entropy Alloy CrMnFeCoNi, *Scr. Mater.*, 2016, **113**, p 106–109

8. B. Schuh, F. Mendez-Martin, B. Völker, E.P. George, H. Clemens, R. Pippan, and A. Hohenwarter, Mechanical Properties, Microstructure and Thermal Stability of a Nanocrystalline CoCrFeMnNi High-Entropy Alloy After Severe Plastic Deformation, *Acta Mater.*, 2015, **96**, p 258–268

9. Y.-K. Kim, Y.-A. Joo, H.S. Kim, and K.-A. Lee, High Temperature Oxidation Behavior of Cr-Mn-Fe-Co-Ni High Entropy Alloy, *Intermetallics*, 2018, **98**, p 45–53

10. C.-H. Tsau, S.-X. Lin, and C.-H. Fang, Microstructures and Corrosion Behaviors of FeCoNi and CrFeCoNi Equimolar Alloys, *Mater. Chem. Phys.*, 2017, **186**, p 534–540

11. H. Lu, Z. Li, A.M. Mingers, and D. Raabe, Corrosion Behavior of an Equiatomic CoCrFeMnNi High-Entropy Alloy Compared with 304 Stainless Steel in Sulfuric Acid Solution, *Corros. Sci.*, 2018, **134**, p 131–139

12. Standard Guide for Determination of Various Elements by Direct Current Plasma Atomic Emission Spectrometry, ASTM E1097-12 (2017)

13. Standard Test Method for Determination of Carbon in Refractory and Reactive Metals and Their Alloys by Combustion Analysis, ASTM E1941-10 (2016)

14. S. Zhang, C.L. Wu, C.H. Zhang, M. Guan, and J.Z. Tan, Laser Surface Alloying of FeCoCrAlNi High-Entropy Alloy on 304 Stainless Steel to Enhance Corrosion and Cavitation Erosion Resistance, *Opt. Laser Technol.*, 2016, **84**, p 23–31

15. M. Vaidya, A. Karati, A. Marshal, K.G. Pradeep, and B.S. Murty, Phase Evolution and Stability of Nanocrystalline CoCrFeNi and CoCrFeMnNi High Entropy Alloys, *J. Alloys Compd.*, 2019, **770**, p 1004–1015

16. W.S. Tait, *An Introduction to Electrochemical Corrosion Testing for Practicing Engineers and Scientists*, Racine, Wisconsin, 1994

17. J.R. Galvele, in *Passivity of Metals*, ed. by R.P. Frankenthal, J. Kruger (The Electrochemical Society, Princeton, 1978), p. 285

18. H.S. Isaacs, U. Bertocci, J. Kruger, and S. Smialowska, (eds.) in *Advances in Localized Corrosion: Proceedings of the Second International Conference on Localized Corrosion*. (Houston, Texas: National Association of Corrosion Engineers, 1990), p. 41

19. G.S. Frankel, Pitting Corrosion of Metals a Review of the Critical Factors, *J. Electrochem. Soc.*, 1998, **145**(6), p 2186–2198

20. P.M. Natishan, W.E. O'Grady, E. McCafferty, D.E. Ramaker, K. Pandya, and A. Russell, Chloride Uptake by Oxide Covered Aluminum as Determined by X-Ray Photoelectron and X-Ray Absorption Spectroscopy, *J. Electrochem. Soc.*, 1999, **146**(5), p 1737–1740

21. L.A. Krebs and J. Kruger, in *Passivity of Metals and Semiconductors*, ed. by M.B. Ives, J.L. Luo, J.R. Rodda (The Electrochemical Society, Pennington, 2001), p. 561

22. D.D. Macdonald, The Point Defect Model for the Passive State, *J. Electrochem. Soc.*, 1992, **139**(12), p 3434–3449

23. E. McCafferty, *Introduction to Corrosion Science*, Springer, Berlin, 2009

24. E. McCafferty, A Competitive Adsorption Model for the Inhibition of Crevice Corrosion and Pitting, *J. Electrochem. Soc.*, 1990, **137**(12), p 3731–3737

25. G. Butler, P. Stretton, and J.G. Beynon, Initiation and Growth of Pits on High-Purity Iron and Its Alloys with Chromium and Copper in Neutral Chloride Solutions, *Br. Corros. J.*, 1972, **7**(4), p 168–173

26. H.-H. Strehblow, Nucleation and Repassivation of Corrosion Pits for Pitting on Iron and Nickel, *Mater. Corros.*, 1976, **27**(11), p 792–799

27. T.J. Glover, Recent Developments in Corrosion-Resistant Metallic Alloys for Construction of Sea-Water Pumps, *Mater. Perform.*, 1988, **27**, p 51–56

28. Y.L. Chou, J.W. Yeh, and H.C. Shih, The Effect of Molybdenum on the Corrosion Behavior of the High-Entropy Alloys $Co_1.CrFeNi_{1.5}Ti_{0.5-}Mo_x$ in Aqueous Environments, *Corros. Sci.*, 2010, **52**, p 2571–2581

29. A.-D. Kamal, K.N. Raymond, and D.P. Freyberg, The Bihydroxide $(H_3O_2-)$ Anion. A Very Short, Symmetric Hydrogen Bond, *J. Am. Chem. Soc.*, 1979, **101**(13), p 3688–3689

30. B.N. Popov, *Corrosion Engineering: Principles and Solved Problems*, Elsevier, Amsterdam, 2015

31. C.P. Lee, Y.Y. Chen, C.Y. Hsu, J.W. Yeh, and H.C. Shih, Enhancing Pitting Corrosion Resistance of $Al_xCrFe_{1.5}MnNi_{0.5}$ High-Entropy Alloys by Anodic Treatment in Sulfuric Acid, *Thin Solid Films*, 2008, **517**, p 1301–1305